Full Length Article

Failure strength and fracture characteristics of rock with discontinuity under indirect tension

Dongya Han [a,b], Jianbo Zhu [c,*], Yat-Fai Leung [b,**]

[a] *School of Resources and Safety Engineering, Central South University, Changsha, China*
[b] *Department of Civil and Environmental Engineering, The Hong Kong Polytechnic University, Hong Kong, China*
[c] *Guangdong Provincial Key Laboratory of Deep Earth Sciences and Geothermal Energy Exploitation and Utilization, Institute of Deep Earth Sciences and Green Energy, College of Civil and Transportation Engineering, Shenzhen University, Shenzhen, China*

ABSTRACT

Large-scale discontinuities can significantly affect the mechanical properties of rock masses. However, the tensile behavior of rock discontinuities is often less investigated. To study the statistical characteristics of failure strength and fracture characteristics of rock discontinuities, Brazilian disc tests were conducted on limestone specimens with a single natural discontinuity at different load-discontinuity angles (β). In this study, $\beta = 0°$ and $\beta = 90°$ correspond to the discontinuity parallel and perpendicular to loading direction, respectively. The results show that Brazilian failure strength (BFS) can reasonably represent the tensile strength of rock with discontinuities, by comparing the BFS and tensile stress in the disc center at peak force. The two-parameter Weibull distribution can capture the statistical BFS characteristics of rock discontinuities parallel to loading direction ($\beta = 0°$) and at different load-discontinuity angles ($\beta \neq 0°$). All specimens with discontinuity at different load-discontinuity angles show more plastic deformational behaviour than intact rock specimen. With increasing β, the mean BFS of limestone with discontinuity increases before reaching a plateau at $\beta = 45°$. The single plane of weakness theory best explains the BFS of fractured limestone with β. Only a specific segment of pre-existing rock discontinuity could affect the fracture process. When $\beta = 0°$, interfacial cracks and alternative cracks formed. When $\beta \neq 0°$, mixed failure mode with shear and tensile failure occurred, particularly when $\beta = 30°$ and $\beta = 60°$. The findings can contribute to better understanding the failure and fracture characteristics of rock with discontinuities, particularly the interaction of pre-existing discontinuities with stress-induced fracturing.

© 2022 Institute of Rock and Soil Mechanics, Chinese Academy of Sciences. Production and hosting by Elsevier B.V. This is an open access article under the CC BY-NC-ND license (http://creativecommons.org/licenses/by-nc-nd/4.0/).

1. Introduction

Most rocks are generally heterogeneous and have random flaw distributions. Flaws can be microcracks within grains and at grain boundaries, and larger-scale discontinuities such as joints (Paterson and Wong, 2005; Zhang, 2010). Because a brittle material's tensile failure is governed by the flaws (Griffith, 1921), the tensile strength ranges widely from specimen to specimen, even if the specimens are of the same material and tested under the same conditions. This can be attributed to the random positions, lengths and orientations of the flaws (Doremus, 1983; Nohut and Lu, 2012; Zhu et al., 2018; Zhou et al., 2019, 2020; Li et al., 2020a, 2021). Therefore, the description of brittle material tensile strength should be incorporated with flaw statistics (Lawn, 1993; Lu et al., 2002). Flaw statistics here means the distribution function for flaw characteristics (flaw size, flaw population, etc.) in a material, including Weibull, normal, log-normal, gamma and generalized exponential distribution functions (Basu et al., 2009; Nohut and Lu, 2012; Ozaki et al., 2018). As rock discontinuities can significantly affect the physical and mechanical properties of rocks under tension (Lee et al., 2015; Shang et al., 2016; Sharafisaf et al., 2019; Han and Yang, 2021), the rock discontinuity's tensile behavior is critically important to the stability of rock masses (Diederichs and Kaiser, 1999; Ghazvinian et al., 2012; Shang et al., 2016). Although recent studies have investigated the tensile strength of rock discontinuities (Shang

---

* Corresponding author.
** Corresponding author.
E-mail addresses: jianbo.zhu@szu.edu.cn (J. Zhu), andy.yf.leung@polyu.edu.hk (Y.-F. Leung).

et al., 2016; Cacciari and Futai, 2018; Han et al., 2020a, 2022), it is still unclear how rock discontinuities in the rock matrix influence the scattering of tensile strength from specimen to specimen, which renders a rather difficult assessment of strength properties. In addition, it is known that the load-discontinuity angle, i.e. inclination angle, could result in significant anisotropy of rock mechanical properties (Lee et al., 2015; Chandler et al., 2016). Thus, it is of great academic interest and engineering significance to perform statistical studies on the tensile fracture and strength anisotropy of fractured rocks.

Probabilistic fracture models are usually used to characterize the strength distributions of brittle materials. The fracture model based on the nucleation of incipient flaws has been widely utilized to investigate rock fracture and strength (e.g. Benz, 1994; Wong et al., 2006; Amaral et al., 2008; Chen et al., 2014), where the flaw size distribution is usually described by the Weibull function (Weibull, 1939). The application of the Weibull distribution to tensile strength variations of intact rock or rock-like materials has been extensively studied. For example, Amaral et al. (2008) conducted bending tests on granite and found that the Weibull distribution can capture the probabilistic features of bending strength. Chen et al. (2014) obtained the tensile strength of concrete by various methods and found that the variations can be accurately described by the Weibull distribution. However, very few efforts have been made to apply the fracture model to characterize the strength distributions of fractured rock.

To investigate the statistical characteristics of strength and fracture behavior of rock discontinuities under tension, Brazilian disc tests were conducted on limestone specimens with a single discontinuity at different load-discontinuity angles. The two-parameter Weibull distribution was used to describe the distribution of failure strength. The interactions of induced fractures with the pre-existing discontinuity at different load-discontinuity angles were also analyzed. The findings in this study facilitate the descriptions of fracture strength of fractured rocks in terms of a reliability function, and provide a rich dataset offering insight into tensile fracture properties of rock with discontinuities.

2. Theoretical background

2.1. Weibull distribution

Weibull (1951) adopted extreme value statistics to characterize the strength variation of materials. Extreme value statistics focus on extreme and rare events, implying that the overall failure is primarily controlled by the weakest elements (Nohut, 2014; Tang and Kaiser, 1998). In practice, the two-parameter Weibull distribution function is preferred for its ease of parameter determination (Nohut, 2014). The cumulative probability of the two-parameter Weibull distribution is expressed as (Wong et al., 2006):

$$F(\sigma) = 1 - \exp\left[-\left(\frac{\sigma}{\sigma_0}\right)^m\right] \qquad (1)$$

and a linear form can be obtained by logarithmic transformation:

$$\ln\left(\ln\frac{1}{1-F(\sigma)}\right) = m\ln\sigma - m\ln\sigma_0 \qquad (2)$$

where m is the Weibull modulus, and σ_0 is the characteristic strength.

As the true value of $F_i(\sigma)$ for a certain specimen is unknown, some estimators have been introduced (e.g. Gurvich et al., 1997; Dirdikolu et al., 2002; Nakamura et al., 2007; Davies, 2017a, b).

Davies (2017a) recommended the following expression as the probability estimator, due to its simplicity and a relatively small coefficient of variation:

$$F_i(\sigma) = \frac{i - A}{N + 1} \quad \left(0 \le A \le 1\right) \qquad (3)$$

where $F_i(\sigma)$ is the probability of the ith value in an ordered set of N strengths (i.e. the number of test specimens), and A is an empirical parameter for determining the probability estimator.

2.2. Tensile strength criteria for rock with weak planes

The ISRM method (ISRM, 1978) inherently assumes that tensile fracture initiates at the disc center. The indirect tensile strength is then calculated by the following formula:

$$\sigma_t = 0.636P_{\max}/(Dt) \qquad (4)$$

where $P_{\max}$ is the diametral load at failure; and D and t are the diameter and thickness of the disc specimen, respectively. For rock with discontinuities of interest in this study, Brazilian failure strength (BFS) rather than tensile strength will be used to present the results of Eq. (4), which is adopted to normalize the failure force to disc diameter and thickness. BFS can realistically reflect the ability of a specimen with discontinuities to resist Brazilian splitting failure (Tavallali and Vervoort, 2010a, b; Roy et al., 2017; Feng et al., 2020). Whether this value can reasonably represent the tensile strength will be discussed in later section.

To predict the tensile strength of rock with weak planes, some criteria have been proposed. For example, the single plane of weakness (SPW) theory (Lee and Pietruszczak, 2015) assumed that tensile strength across the weak plane is, in general, much lower than that of the rock material. As a result, tensile fracturing is likely to occur along this weak plane if its inclination is less than a critical value (β^*). Lee and Pietruszczak (2015) expressed the tensile strength as

$$\sigma_t(\beta) = \begin{cases} \dfrac{\sigma_{tb}}{\cos^2\beta} & (0° \le \beta \le \beta^*) \\[2mm] \sigma_{tm} & (\beta^* \le \beta \le 90°) \end{cases} \qquad (5)$$

where $\sigma_t(\beta)$ denotes the tensile strength of a specimen at β; σ_{tm} and σ_{tb} represent the tensile strengths of the rock matrix and weak plane, respectively; and $\beta^* = \cos^{-1}\sqrt{\sigma_{tb}/\sigma_{tm}}$.

To identify an appropriate criterion for this study, other tensile strength criteria are also considered, including the Hobbs–Barron (H–B) criterion (Hobbs, 1967; Barron, 1971):

$$\sigma_t(\beta) = \begin{cases} \dfrac{2\sigma_{tb}}{\cos\beta(1+\cos\beta)} & (0° \le \beta \le \beta^*) \\[2mm] \sigma_{tm} & (\beta^* \le \beta \le 90°) \end{cases} \qquad (6)$$

with $\cos\beta^*(1+\cos\beta^*) = 2\sigma_{tb}/\sigma_{tm}$.

Additionally, the Nova–Zaninetti (N–Z) criterion (Nova and Zaninetti, 1990) is given as follows:

$$\sigma_t(\beta) = \frac{\sigma_{tb}\,\sigma_{tm}}{\sigma_{tb}\sin^2\beta + \sigma_{tm}\cos^2\beta} \qquad (7)$$

and the Lee–Pietruszczak (L–P) criterion (Lee and Pietruszczak, 2015) is represented by

$$\sigma_t(\beta) = \frac{\sigma_{tm} + \sigma_{tb}}{2} - \frac{\sigma_{tm} - \sigma_{tb}}{2}\cos(2\beta) \qquad (8)$$

3. Specimen preparation and test set-up

This study used Jingxing limestone from the Hebei Province, China. All the limestone specimens here are recrystallized dolomite sparry oolitic limestones. The compressive strength, elastic modulus and Poisson's ratio of the limestone are 171.4 MPa, 75.5 GPa and 0.32, respectively (Han et al., 2020b). Stylolites are irregular planes of discontinuity and ubiquitous geo-patterns observed in the upper crust, from geological reservoirs in sedimentary rocks to deformation zones, in folds, faults, and shear zones (Vandeginste and John, 2013; Toussaint et al., 2018). Stylolites are often filled with insoluble materials such as organic matter, oxides or clay particles (Nelson, 1981; Nicolas, 1987). In this study, the stylolites were used as the sealed or healed fractures. Consequently, the tensile behavior of fractures that have bonding strength can be studied. Because of local dissolution along the stylolite, the removed material may provide the cement that precipitates in the host rock surrounding the stylolites. Therefore, stylolite has bonding strength, contributing to the tensile bearing capacity. Additionally, stylolite is a natural rock–rock interlocked interface (Toussaint et al., 2018), which also provides some bonding strength. For the sake of simplicity, the limestone with a discontinuity is referred to 'fractured limestone' in subsequent sections. The thickness of stylolites varies from 0.5 mm to 2.8 mm.

The specimens were cored from the limestone blocks and cut and carefully polished to ensure that each disc is 24 mm (± 0.05 mm) thick and 48.05 mm (± 0.05 mm) in diameter. The intact disc specimen density is (2722 $\pm$ 34) kg/m^3. The fractured disc specimen density is (2715 $\pm$ 20) kg/m^3, which is almost identical to that of intact limestone. Fig. 1 shows some of the specimens used in this study. For the disc specimens shown in Fig. 1a, the discontinuity is located approximately in the disc center and parallel to the loading direction, i.e. the discontinuity-load inclination angle $\beta = 0°$. Meanwhile, Fig. 1b shows an example where $\beta \neq 0°$. Note that the discontinuities do not always pass through the disc center, and the distance to the disc center (d) also varies. This is due to the three-dimensional (3D) nature and

randomness of natural discontinuity orientation. The number of specimens for each testing condition was not the same because a significant number of fractured specimens broke during the drilling, cutting and polishing processes. The intact Brazilian specimen is named 'BI', as listed in Table 1. The specimen numbers BN-0, BN-30, BN-45, BN-60, BN-75, and BN-90 in Table 2 denote the Brazilian disc tests conducted on the specimens at discontinuity-load angles of 0°, 30°, 45°, 60°, 75°, and 90°, respectively.

Fig. 2 shows a schematic diagram of the testing system used in this study. A displacement-controlled machine (VJ Tech machine) with a low loading capacity of 100 kN was used to conduct the Brazilian tests. The loading rate was controlled at 0.3 mm/min. This Brazilian test procedure was described in detail by Mellor and Hawkes (1971) and ISRM (1978). A disc-shaped rock specimen was loaded by standard Brazilian jaws coupled with two guide pins. The arc of contact was approximately 10° at failure, i.e. $2\alpha = 10°$. During the Brazilian test, the specimen was wrapped with a soft heat-shrink tube to improve the contact condition. The diameter of the tube was slightly larger than that of the disc specimen, and the role of the tube was similar to that of the adhesive paper strip or masking tape (ISRM, 1978; Erarslan and Williams, 2012). A strain gauge with a length of 10 mm was firmly glued at the disc center to record the horizontal strain (tensile strain). In addition, a high-speed camera, Photron FASTCAM SA-Z, was used to capture the fracture process during the tests. The frame rate was 2000 frames per second with a resolution of 256 × 256 pixels.
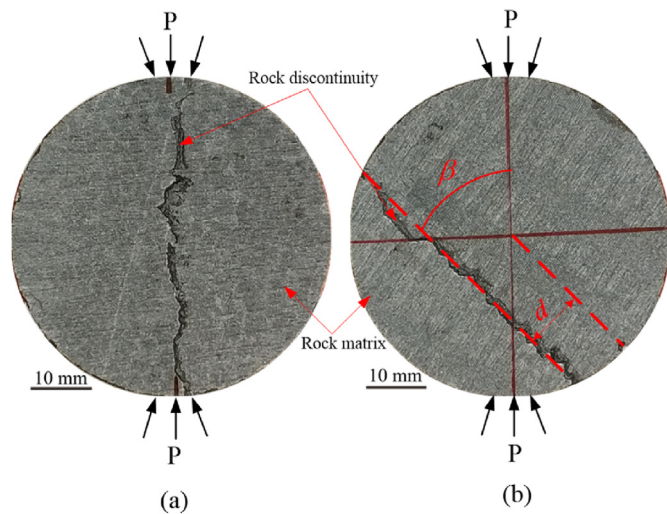
4. Testing results and analysis

4.1. BFS

4.1.1. Effect of inclination angle on BFS

The tensile strengths of intact specimens are listed in Table 1. The mean tensile strength of intact limestone is (13.01 $\pm$ 1.12) MPa.

Fig. 1. Brazilian disc specimens with: (a) A discontinuity located approximately in the disc center (inclination angle $\beta = 0°$); and (b) A discontinuity located at a certain angle with the loading direction ($\beta \neq 0°$). P is the diametrical compressive loading. d is the distance of the discontinuity to the disc center.

Table 1
Testing results of intact limestone specimens.

Specimen	P_{max} (kN)	BFS (MPa)	Failure strain (10^{-6})
BI-1	22.72	12.54	476.9
BI-2	27.02	14.91	457.67
BI-3	26.68	14.73	405.75
BI-4	26.95	14.88	512.48
BI-5	25.61	14.14	517.29
BI-6	20.7	11.43	373.06
BI-7	24	13.25	436.52
BI-8	21	11.59	429.79
BI-9	21.99	12.14	499.02
BI-10	23.56	13.01	467.29
BI-11	24.18	13.35	437.48
BI-12	20.88	11.53	503.83
BI-13	19.66	10.85	497.1
BI-14	26.39	14.57	511.52
BI-15	22.05	12.17	451.9
BI-16	25.4	14.02	454.79
BI-17	25.75	14.22	454.79
BI-18	23.6	13.03	437.48
BI-19	22.21	12.26	465.37
BI-20	22.77	12.57	472.1
BI-21	24.94	13.77	429.79
BI-22	21.91	12.1	469.21
BI-23	23.47	12.96	-
BI-24	22.82	12.6	475.94
BI-25	24.14	13.33	522.09
BI-26	22.14	12.22	462.48
BI-27	23.83	13.15	454.79

Note: P_{max} is the maximum diametral load. BFS is the Brazilian failure strength determined by Eq. (4). The failure strain is the tensile strain at the failure load. '-' indicates that the value cannot be determined from the test because of the catastrophic failure of the specimen.

Table 2
Testing results of fractured limestone specimens under indirect tension.

Specimen	P_{max} (kN)	BFS (MPa)	Failure strain (10^{-6})	Specimen	P_{max} (kN)	BFS (MPa)	Failure Strain (10^{-6})
BN-0-1	10.66	5.89	600.94	BN-30-9	16.7	9.23	208.65
BN-0-2	10.21	5.64	1344.18	BN-30-10	26.37	14.57	352.87
BN-0-3	6.88	3.8	2452.79	BN-30-11	22.28	12.31	220.18
BN-0-4	13.5	7.46	1167.26	BN-30-12	15.25	8.43	230.76
BN-0-5	13.73	7.59	541.32	BN-30-13	19.22	10.62	786.51
BN-0-6	16.5	9.12	183.65	BN-30-14	13.07	7.22	128.84
BN-0-7	11.8	6.52	192.3	BN-30-15	16.97	9.38	468.25
BN-0-8	16.32	9.02	138.46	BN-30-16	22.42	12.39	231.72
BN-0-9	17.21	9.51	184.61	BN-30-17	18.04	9.97	156.72
BN-0-10	17.72	9.79	517.29	BN-30-18	21.52	11.89	210.57
BN-0-11	17.43	9.63	236.53	BN-30-19	6.55	3.62	99.03
BN-0-12	14.13	7.81	212.49	BN-30-20	14.22	7.86	145.19
BN-0-13	15.98	8.83	274.99	BN-45-1	20.79	11.49	437.48
BN-0-14	12.96	7.16	730.74	BN-45-2	22	12.16	442.29
BN-0-15	16.34	9.03	340.37	BN-45-3	24.86	13.74	533.63
BN-0-16[a]	5.36	2.96	1817.23	BN-45-4	22.8	12.6	499.98
BN-0-17[a]	4.52	2.5	52.88	BN-45-5	20.18	11.15	295.18
BN-0-18	11.31	6.25	173.07	BN-60-1	22.98	12.7	405.75
BN-0-19	14.95	8.26	772.08	BN-60-2	21.12	11.67	410.56
BN-0-20	14.33	7.92	186.53	BN-60-3	23.76	13.13	348.06
BN-0-21	10.71	5.92	100.96	BN-60-4	14.57	8.05	440.37
BN-0-22	8.25	4.56	216.34	BN-60-5	24.99	13.81	551.9
BN-0-23	9.7	5.36	104.8	BN-75-1	23.04	12.73	471.14
BN-0-24	22.57	12.47	304.8	BN-75-2	20.97	11.59	353.83
BN-0-25	12.00	6.63	151.92	BN-75-3	24.79	13.87	524.02
BN-0-26	17.35	9.59	230.76	BN-75-4	16.85	9.31	242.3
BN-0-27	12.58	6.95	1140.34	BN-75-5	23.45	12.96	390.37
BN-0-28	17.41	9.62	293.26	BN-90-1	23	12.71	356.72
BN-0-29	13.19	7.29	228.84	BN-90-2	19.89	10.99	277.87
BN-0-30[a]	6.59	3.64	1367.25	BN-90-3	20.38	11.26	436.52
BN-0-31	17.77	9.82	215.38	BN-90-4	24.79	13.7	421.14
BN-0-32	13.66	7.55	821.12	BN-90-5	26.65	14.73	380.75
BN-0-33	15.85	8.76	250.95	BN-90-6	19.71	10.89	365.37
BN-0-34	22.11	12.22	261.53	BN-90-7	24.83	13.72	399.02
BN-0-35	12.56	6.94	1603.78	BN-90-8	22.55	12.46	357.68
BN-30-1	22.08	12.2	504.79	BN-90-9	18.2	10.06	520.17
BN-30-2	16.47	9.1	374.98	BN-90-10	20.39	11.27	451.9
BN-30-3	19.69	10.88	546.13	BN-90-11	25.44	14.06	446.14
BN-30-4	18.11	10.01	438.44	BN-90-12	22.33	12.34	276.91
BN-30-5	21.79	12.04	521.13	BN-90-13	26.96	14.9	329.79
BN-30-6	16.36	9.04	441.33	BN-90-14	19.6	10.83	157.69
BN-30-7	23.61	13.05	372.1	BN-90-15	22.31	12.33	312.49
BN-30-8	24.23	13.39	299.99				

[a] The specimen broke along the interface, as shown in the later section.

The BFSs of specimens with discontinuity are listed in Table 2. Fig. 3 shows the relationship between the BFS of fractured
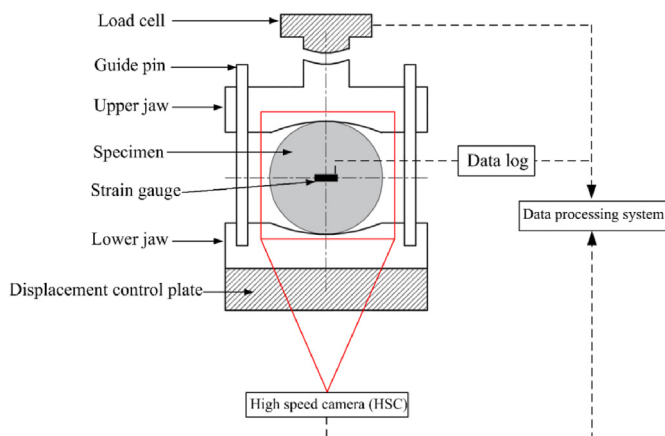

Fig. 2. Diagram of the testing system for the Brazilian disc test.

limestone and the inclination angle β, with error bars indicating the standard deviation (SD). As shown in Fig. 3, the BFS of fractured limestone is lower than that of intact limestone, and increases with the inclination angle from $\beta = 0°$ to $\beta = 45°$. However, from $\beta = 45°$ to $\beta = 90°$, the BFS remains almost constant, approaching that of intact limestone. Data scattering is observed for the BFS of fractured limestone, and is the most pronounced when $\beta = 0°$ with a corresponding coefficient of variation of 31.3%. The coefficients of variation for $\beta = 30°$, $\beta = 45°$, $\beta = 60°$, $\beta = 75°$, and $\beta = 90°$ are 18.96%, 8.34%, 19.1%, 14.52%, and 12.32%, respectively, which are significantly smaller than that for $\beta = 0°$.

It is interesting to find that the dependence of fractured limestone specimen BFS on the load-discontinuity inclination angle is similar to some transversely isotropic rocks (Lee and Pietruszczak, 2015; Ma et al., 2018). Therefore, the test data in this study are interpreted with the tensile strength criteria originally developed for transversely isotropic rocks. In addition to test data, Fig. 3 also shows the predicted values of the BFS using different criteria. Note that the values of $\sigma_{tb} = 7.49$ MPa (BFS at $\beta = 0°$) and $\sigma_{tm} = 12.15$ MPa (mean BFS from $\beta = 45°$ to $\beta = 90°$) were used, and consequently, the critical angles equal 38.29° and 44.16° for the SPW and H−B criteria, respectively. For the N−Z and L−P criteria, the curves were obtained by best fitting the data points, with $\sigma_{tb} = 9.51$ MPa and $\sigma_{tm} = 16.82$ MPa for the L−P criterion, and $\sigma_{tb} = 9.22$ MPa and $\sigma_{tm} = 12.82$ MPa for the N−Z criterion. To some extent, all these criteria appear to be applicable for limestone with a single discontinuity, but the SPW criterion appears to agree best with the test data. To quantify the goodness-of-fit, the standard error was calculated by

$$SE = \sqrt{\frac{\sum (\sigma_{tP}(\beta) - \sigma_{tE}(\beta))^2}{n}} \tag{9}$$

where $\sigma_{tE}(\beta)$ and $\sigma_{tP}(\beta)$ are the experimental value and the corresponding predicted value at β, respectively; and n is the number of data points. A lower SE illustrates a better match.

The calculated SE values are 0.34, 1.02, 0.61 and 1.17 for the SPW, N−Z, H−B, and L−P criteria, respectively. If the same values of $\sigma_{tb} = 7.49$ MPa and $\sigma_{tm} = 12.15$ MPa were also used for the N−Z
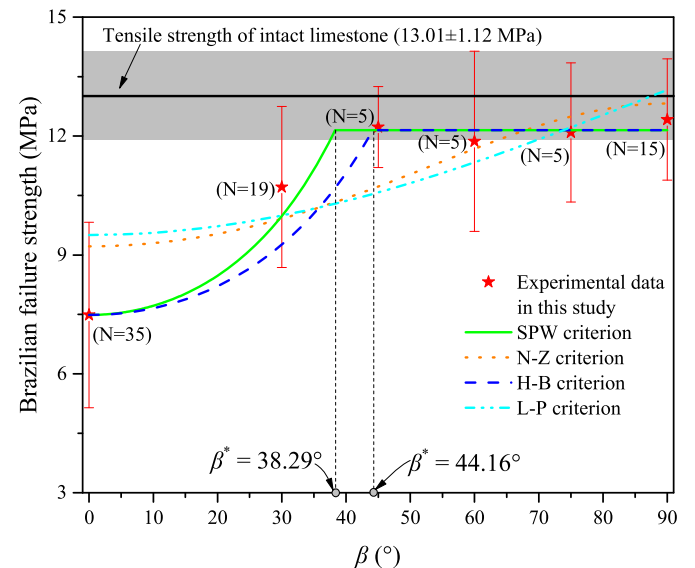

Fig. 3. BFSs obtained by experiments (mean value ± SD) and those predicted by different criteria at different values of β. Refer to the text for details of the criteria. β^* is the critical angle used in SPW and H−B criteria. N is the number of specimens.

and L−P criteria, *SE* would become 1.67 and 2.9, respectively, showing a much lower accuracy. *SE* is the smallest when the SPW criterion was adopted. For limestones with a single discontinuity used in this study, the SPW criterion is recommended to capture the anisotropy of BFS at various β values.

4.1.2. BFS distribution

To apply the Weibull distribution to the test results, *N* recorded BFSs were ranked in ascending order for the intact limestone specimens and fractured limestone specimens with $\beta = 0°$, 30°, and 90°. In this study, the cumulative probability of failure is assigned according to $F_i(\sigma) = i/(N + 1)$, i.e. $A = 0$ in Eq. (3). This estimator has been widely used for rocks or rock-like materials (Gurvich et al., 1997; Chen et al., 2014, 2015). The Weibull parameters *m* and σ_0 were determined for each testing condition by fitting the experimental data with the linearized form, i.e. Eq. (2).

Fig. 4 shows the linearized Weibull plots of BFS for intact specimens and fractured specimens with $\beta = 0°$, 30°, and 90°. The Weibull modulus *m* is the slope of the linear function, and the characteristic strength σ_0 is determined from the intercept. Larger values of *m* suggest more homogeneous materials, while smaller values suggest more heterogeneous materials. The fitting results are listed in Table 3. R^2 is above 0.93 for all measurement sets, indicating that the linearized Weibull distribution gives a good approximation of the experimental data. It is herein concluded that the BFS distribution can be captured by the Weibull distribution with two parameters *m* and σ_0. Fig. 5 shows the cumulative probability plots of BFSs using the parameters listed in Table 3, which again reveals that the two-parameter Weibull distribution results in a good match with the experimental data.

As stated previously, the numbers of specimens for different β were not the same because of difficulties in specimen preparation. However, the number of specimens may affect the determination of Weibull parameters (Gorjan and Ambro, 2012; Nohut, 2014). Therefore, the effects of the number of test specimens (*N*) on the Weibull modulus and characteristic strength were herein studied. For a certain *N*, the corresponding number of BFS data points was randomly selected from the full dataset where $\beta = 0°$ and ranked in ascending order. Then, using Eq. (2), the most suitable

Table 3
Weibull parameters for different limestone specimens under indirect tension.

Condition	*m*	σ_0 (MPa)	R^2
$\beta = 0°$	3.06	8.43	0.97
$\beta = 30°$	5.53	11.57	0.97
$\beta = 90°$	8.29	13.12	0.93
Intact limestone	12.73	13.52	0.93

Fig. 5. Weibull cumulative distributions of intact and fractured specimen BFSs. The points indicate the experimental measurements. The curves are the cumulative probability function, i.e. Eq. (1), plotted with the Weibull parameters listed in Table 3.

distribution function and hence the Weibull parameters can be determined. This procedure was repeated 10 times for each *N*. The $\beta = 0°$ dataset was chosen since it contains the largest amount of test data. In addition, the Weibull modulus at this angle is the smallest, implying a broader distribution of BFS. As a result, greatest scattering is expected in this dataset.

Fig. 6 shows the effect of the number of specimens on the Weibull modulus *m* and characteristic strength σ_0. The error bar represents the SD of *m* and σ_0. The mean values of *m* and σ_0 are close to the 'true' values from the full dataset where *N* = 35. With an increasing value of *N*, the SD decreases. When *N* > 25, the SD is reduced, as shown in Fig. 6. Therefore, the Weibull parameters estimated from different numbers of specimens at different values of β are, to some extent, comparable.

The Weibull modulus of intact limestone is 12.73 in this study, which is within the range for intact limestones previously reported by Grange et al. (2008). The results listed in Table 3 reveal that *m* for fractured specimens with $\beta = 0°$ is 3.06, which is significantly smaller than that for intact specimens, implying a broader or more heterogeneous nature of fractured limestone BFS with $\beta = 0°$. As *m* is related to the microscale flaw length distribution in a material (Jayatilaka and Trustrum, 1977; Wong et al., 2006), it is postulated that the presence of the larger-scale fracture (the discontinuity) is likely to affect the microscale flaw length distribution. The fitting results also indicated an increase in *m* with increasing β. This is probably due to the discrepancy in the length of the discontinuity in different specimens. It is observed that the discontinuity where $\beta = 0°$ is generally longer than those where $\beta \neq 0°$, as most discontinuities in the former case crossed the disc center, whereas most discontinuities where $\beta \neq 0°$ did not. In addition, the
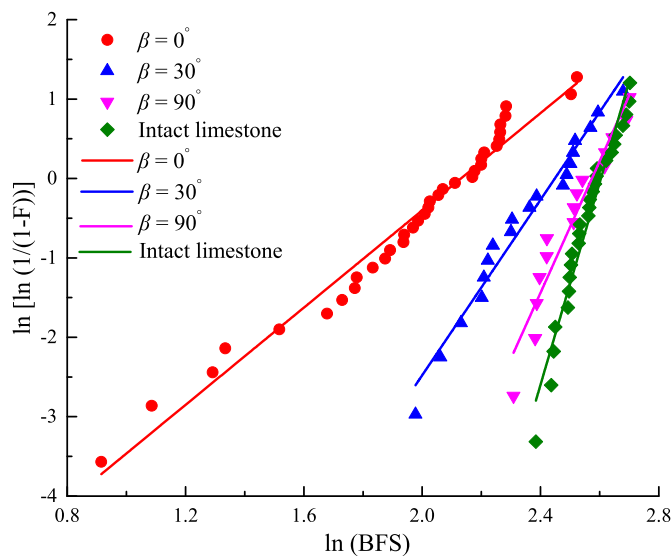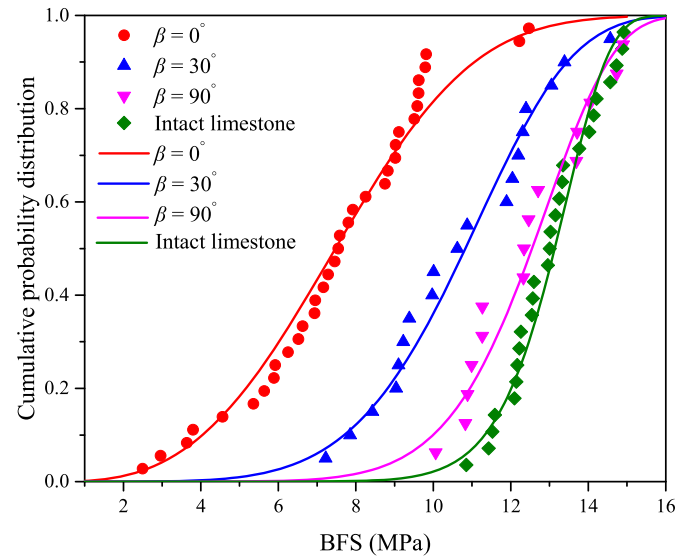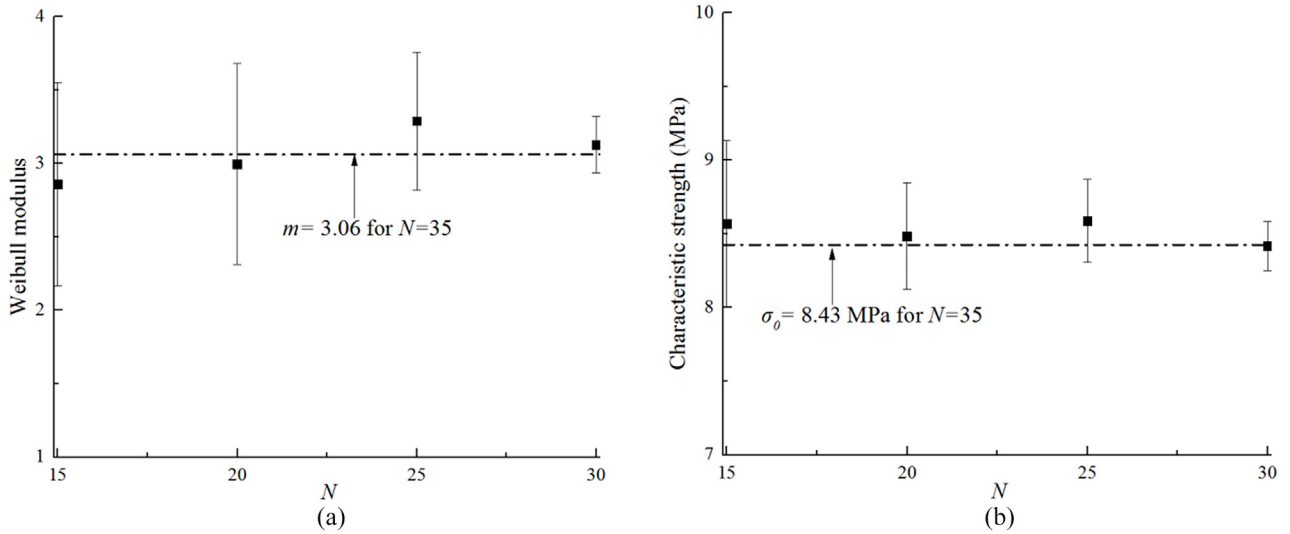

Fig. 4. Weibull plots of intact and fractured specimen BFSs. The points indicate the experimental measurements. The linear function obtained by the best-of-fit is the linear form of Weibull distribution, i.e. Eq. (2).

Fig. 6. Effects of the number of specimens on: (a) Weibull modulus m (mean value ± SD); and (b) Characteristic strength σ_0 (mean value ± SD).

interactions of the induced fracture with the pre-existing discontinuity can be a controlling factor for the BFS distribution. The characteristic strength σ_0 is reduced when the discontinuity is present, and it increases with the increase of β, which is probably induced by different average flaw sizes (Grange et al., 2008).

4.2. Deformation behavior

Fig. 7 shows the typical diametral force versus strain curves for intact and fractured limestone specimens from Brazilian disc tests. In general, the intact limestone specimens showed a linear force−strain behavior in the tested stress range. The force−strain curves for fractured specimens are, however, nonlinear, implying that the fractured specimens showed more plastic behavior. This is similar to observations during static direct tension tests (Han et al., 2020b). Apart from the invisible microcracks formed during the test (Han et al., 2020a), this nonlinearity may be caused by the nonlinear deformation of insoluble materials. Deformation behavior may also be influenced by pre-existing macrofractures associated with cemented interfaces between host rocks and insoluble materials, which influence the deformation behavior. In addition, an increase in porosity was reported in the vicinity of stylolites (Heap et al., 2014; Ebner et al., 2010) and consequently affected the elastic properties (Eberli et al., 2003), which may also be responsible for this nonlinearity.

However, for specimens with the discontinuity not crossing the disc center (Fig. 1b), the stress−strain curve showed a similar pattern to that of intact limestone specimens. For example, the stress−strain curve for specimen BN-30-8 in Fig. 7 shows a linear behavior. This is because the strain gauge was glued at the disc center, and the strains obtained from the strain gauge are in fact those of the rock materials.

The failure strains at the peak load for all specimens are summarized in Tables 1 and 2. Intact limestone failure strain varied from 0.0373% to 0.0522%, with strain anisotropy of 32%. The strain anisotropy here is defined as

$$AI_\varepsilon = \frac{\varepsilon_{\max} - \varepsilon_{\min}}{\varepsilon_{\text{mean}}} \times 100\% \tag{10}$$

where $\varepsilon_{\max}$, $\varepsilon_{\min}$ and $\varepsilon_{\text{mean}}$ are the maximum, minimum and mean failure strains of each dataset, respectively.
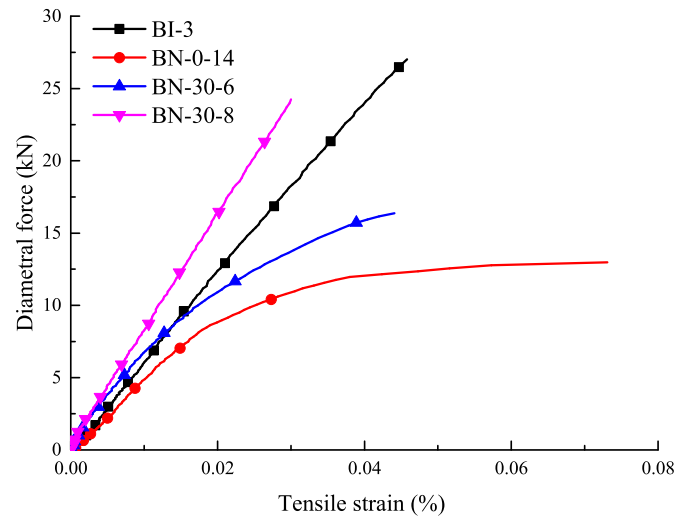

Fig. 7. Typical diametral force vs. tensile strain curves for intact and fractured limestone specimens from Brazilian disc tests.

The fractured specimen failure strain varied from 0.0052% to 0.2452%, showing remarkably higher anisotropy effects than the intact limestone specimens.

4.3. Crack path

The crack path plays a significant role in the discontinuity fracture behavior (Akisanya and Fleck, 1992; Lane, 2003). To study how the induced fracture interacts with the pre-existing discontinuity, crack paths were analyzed with the aid of a high-speed camera.

Fig. 8 shows some typical intact limestone crack paths during the Brazilian disc tests. The diametral cracks (tensile cracks or main cracks) that developed along the loading direction are clearly visible. This can be attributed to the intact limestone specimen homogeneity, which results in a relatively large Weibull modulus.

Fig. 9 shows two types of fractured limestone specimen crack paths with $\beta = 0°$ during the Brazilian disc tests. Observations of the induced crack indicated that the insoluble materials thickness
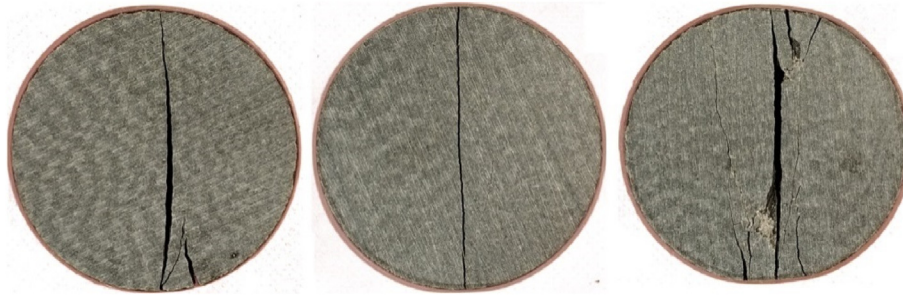
Fig. 8. Some typical fractured intact limestone specimens after the Brazilian disc tests. The disc diameter is 48 mm.
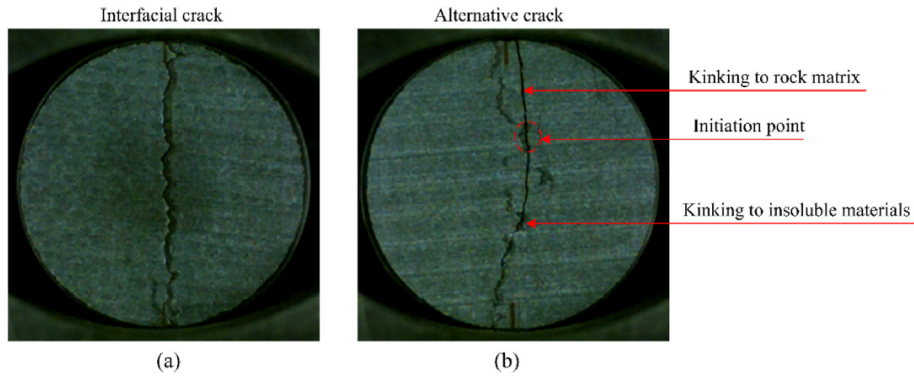

Fig. 9. Typical crack paths of fractured limestone during the Brazilian disc tests where $\beta = 0°$: (a) Interfacial crack; and (b) Alternative crack.

and the discontinuity roughness should be responsible for such differences in the crack paths. The interfacial crack represents debonding between the host rock and insoluble materials, as shown in Fig. 9a. This implies that fractured limestone failure is likely controlled by the interfacial fracture intensity factor. When the test specimens experienced only pure interfacial cracks, lower BFSs were observed, as marked with an asterisk (*) in Table 2. The

alternative crack, as shown in Fig. 9b, initiated from a specific segment of the interface, and then kinked to the host rock and/or insoluble materials. It is therefore suggested that the crack initiation is again controlled by the interfacial fracture intensity factor, while the propagation may be controlled by the stress intensity factors of the host rock and/or insoluble materials around the specific segment of the interface.
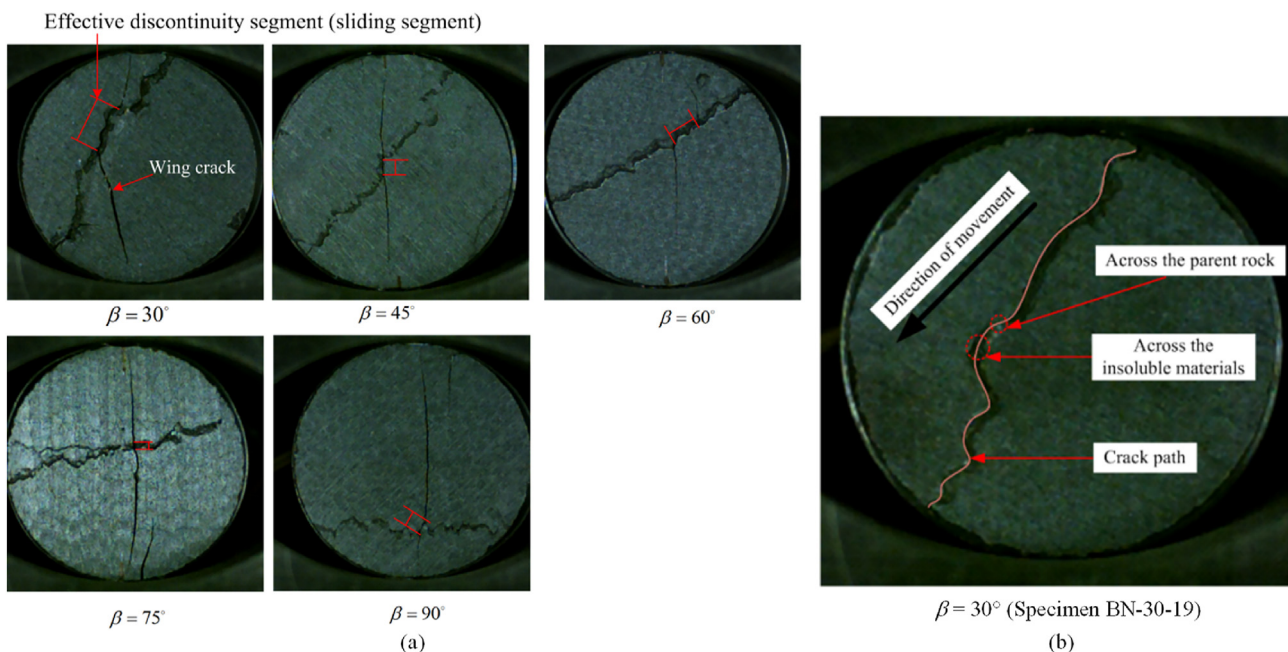

Fig. 10. Typical crack paths of specimens with a discontinuity during the Brazilian disc tests where $\beta \neq 0°$: (a) Wing cracks; and (b) No wing cracks (pure shear failure).

Fig. 10 shows the crack paths for specimens with discontinuity when $\beta \neq 0°$ during the Brazilian disc tests. Fig. 10a shows that almost all the fractured limestone specimens failed in a similar manner, and that although the pre-existing discontinuity crosscuts the specimen, there is only a specific segment of the discontinuity that affects the fracture behavior. This specific segment is defined in this study as the effective discontinuity segment. This effective discontinuity segment first experienced a shear failure resulting from the local shear stress (strain) concentration. The shear behavior was identified by the relative movement of the two separated parts of the disc captured by images by the high-speed camera. The sliding of infilled flaws subject to diametral-compressive load was also reported in a recent investigation with the digital image correlation technique (Sharafisaf et al., 2019). However, it should be noted that in some tests, the effective discontinuity segment may also fail in tension, as demonstrated in Fig. 10a at $\beta = 75°$. As the failure process was fast, it was difficult to capture the entire fracture process with the high-speed camera. Wing cracks were produced at the tips of the sliding segment because of tensile stress (strain) concentration. This implies that the effective discontinuity segment plays a role in transferring the stress (strain) concentration from shear mode to tensile mode. The wing cracks kinked to the rock matrix and propagated in a curved path, starting their extension from the tips and continuing towards the loading points. A similar phenomenon was also observed during the Brazilian disc tests in disc-shaped specimens with a pre-existing flaw (Haeri et al., 2014; Sharafisaf et al., 2019).

There is only one specimen that experienced a shear failure mode at $\beta = 30°$ (specimen BN-30-19), as shown in Fig. 10b. Compared with the other specimens, no induced wing cracks were observed. This is probably because the shear strength of the discontinuity in this specimen is lower, and consequently, the shear

crack cannot be diverted and kinked into the rock matrix. The findings from rock with multiple weak planes may provide evidence for understanding this failure pattern. Pure shear failure does occur when the shear strength of weak planes is low (Tan et al., 2015).

5. Comparisons between BFS and tensile stress of disc center at failure

It is noted that the induced fracture in a significant number of specimens did not pass through the center of the disc specimen, especially for fractured specimens with the discontinuity-load inclination angle $\beta \neq 0°$. This may challenge the applicability of Eq. (4) to calculate the tensile strength in fractured specimens. To examine whether the ISRM (1978) suggested equation, i.e. Eq. (4), is a reasonably accurate approximation of fractured rock specimen tensile strength, a numerical Brazilian disc test using the 3D particle flow code (PFC3D) was further conducted on specimens with the same dimension as those in the experiments, as shown in Fig. 11. The numerical test allows comparisons of the strength determined by Eq. (4) with the tensile stress at the disc center when the peak force was reached.

To simulate rock with discontinuities, two stages should be performed: (1) modeling of the rock matrix; and (2) modeling of the rock matrix with discontinuities. Rock matrix is an assembly of rigid bonded particles, such as blocks or spheres, in 3D in the particle-based discrete element modeling. Based on previous studies (e.g. Li et al., 2020b, 2022), the flat-joint contact (FJC) model is used to model rock matrix because it can surmount the three intrinsic problems raised by the contact-bond or parallel-bond contact model: (1) linear strength envelope, (2) low ratio of uniaxial compressive strength to tensile strength, and (3) low internal
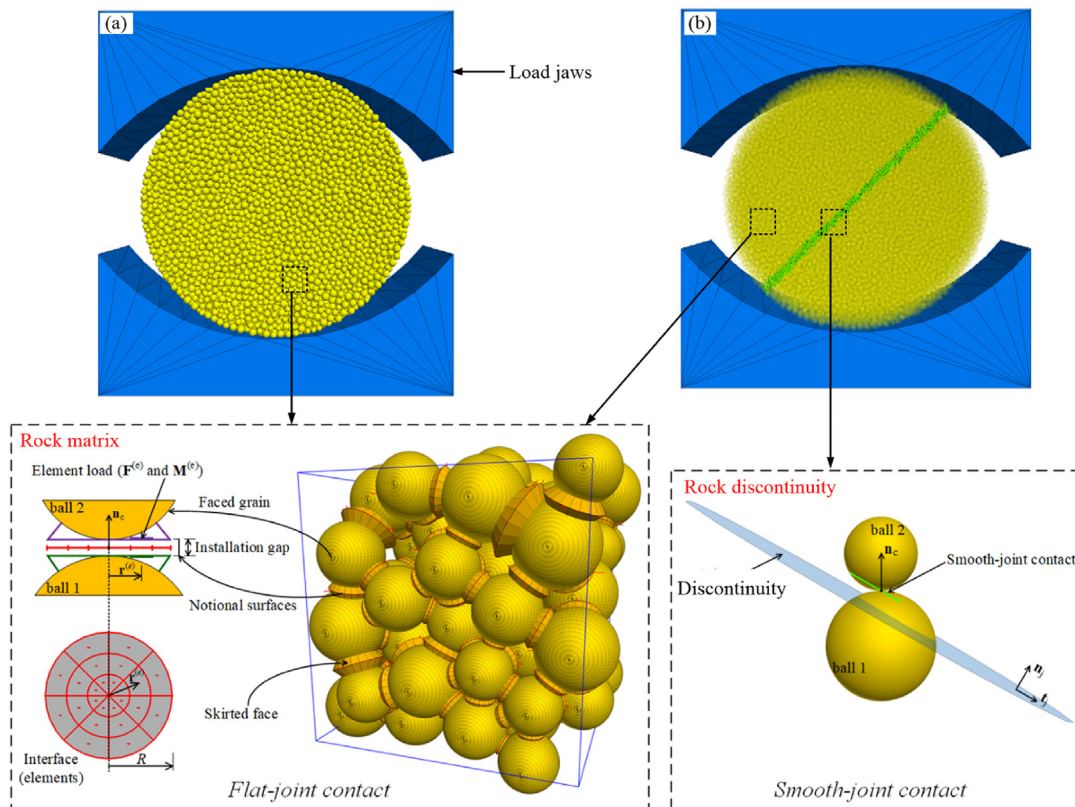

Fig. 11. Numerical models of Brazilian disc tests on (a) intact specimen and (b) specimen with a discontinuity.
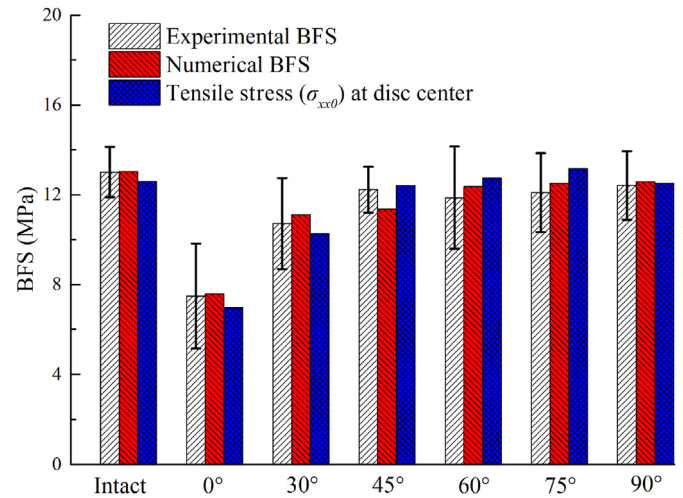
Table 4
Microparameters of the flat and smooth joint models for the rock and the discontinuity.

Materials	Parameters	Value
Rock	Bulk density (kg/m^3)	2720
	Minimum particle radius (mm)	0.5
	Ratio of maximum to minimum particle radius	1.5
	Installation gap ratio	0.3
	Number of elements in radial direction	1
	Number of elements in circumferential direction	4
	Bonded element fraction	0.9
	Gapped element fraction	0
	Effective modulus of bond (GPa)	105
	Ratio of bond normal to shear stiffness	4.5
	Mean bond tensile strength ± SD (MPa)	34 ± 6.8
	Mean bond cohesion strength ± SD (MPa)	420 ± 84
	Friction angle of bond (°)	0
	Friction coefficient of bond	0.2
	Effective modulus of particle contact (GPa)	105
	Ratio of particle normal to shear stiffness	4.5
	Friction coefficient of particle	0.2
Discontinuity	Normal stiffness (GPa/mm)	5.8
	Shear stiffness (GPa/mm)	5.8
	Tensile strength (MPa)	4.75
	Cohesion (MPa)	13
	Friction coefficient	0.7

Fig. 12. Comparison of experimental and numerical BFSs and tensile stress at the disc center when peak force was achieved. BFSs are calculated by Eq. (4). Numerical BFS and tensile stress σ_{xx0} are obtained from the numerical test.

friction angle in reproducing hard rock mechanical behaviors. The behavior of weak planes, i.e. the discontinuity in this study, is modeled using the smooth-joint contact (SJC) model developed by Mas Ivars et al. (2011). The SJM has been adopted successfully in simulating the mechanical behavior of rock discontinuities (Bahaaddini et al., 2013a, b; Yang et al., 2015; Xu et al., 2018). The SJC presents a catastrophic failure, while the FJC shows a progressive failure. In addition, the SJC does not resist the relative rotation (Mas Ivars et al., 2011). Detailed descriptions of FJM and SJM models, such as the strength envelope and force–displacement relationship, can be found in Mas Ivars et al. (2011).

A disc specimen (diameter = 48 mm and thickness = 24 mm) and a cylindrical specimen (diameter = 50 mm and length = 100 mm) were generated, consisting of 26,546 and 119,931 particles connected by FJCs, respectively. The specimens' porosity was fixed at 39.2% using the particle deletion method to eliminate the effect of porosity on strength and elasticity (Li et al., 2018). The same particle size distribution was used for the two specimens, with a maximum to minimum particle diameter ratio of 1.5. The behavior of rock with a discontinuity under indirect tension was modeled by inserting a weak plane at different load-discontinuity angles into the rock matrix. After inserting the weak plane, the FJCs are assigned as the SJCs between particles lying on opposite sides of a discontinuity plane, and the pre-existing bonds are removed at the corresponding positions. In addition, the experimental load jaws were built with the computer-aided design and imported in the numerical model to ensure that the contacts between the load jaw and specimen are the same with the experiment. The numerical specimens generated for Brazilian disc tests are shown in Fig. 11.

The micro-properties of FJC and SJC for reproducing the rock with and without a discontinuity were calibrated against the experimental results obtained from uniaxial compression tests on the cylindrical specimen and Brazilian disc tests on the disc specimens without and with a discontinuity at different load-discontinuity angles. Note that the mean value of experimental BFSs of specimen with/without discontinuities at different discontinuity angles was taken as the basis for calibration. The loading velocity was maintained at 0.015 m/s, which has been proved to be slow enough to promise a quasistatic equilibrium for each step within the specimen (Li et al., 2020b). The calibration of microparameters in this study follows the procedures proposed by Li et al. (2020b). The calibration steps are briefly listed as follows: (1) adjusting the bond tensile strength and conducting Brazilian disc test to match the Brazilian tensile strength; (2) adjusting the bond and particle moduli, the bond cohesion and tensile strength, the ratios of bond and particle normal to shear stiffness and
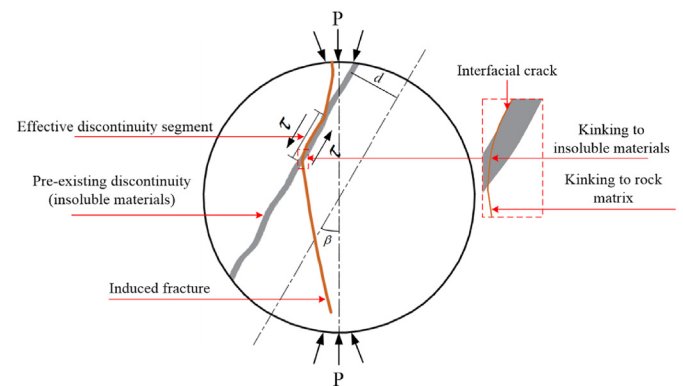
Fig. 13. Diagram of fracture pattern subject to diametral load where $\beta \neq 0°$. τ is the local shear stress.

Table 5
Comparisons between experimental and numerical results of intact rock specimens.

| Uniaxial compressive strength			Poisson's ratio			Young's modulus			Brazilian tensile strength		
Experimental (MPa)	Numerical (MPa)	Error (%)	Experimental	Numerical	Error (%)	Experimental (GPa)	Numerical (GPa)	Error (%)	Experimental (MPa)	Numerical (MPa)	Error (%)
171.4	167.5	2.28	0.32	0.31	3.13	75.5	74	1.99	13.01	13.03	0.15
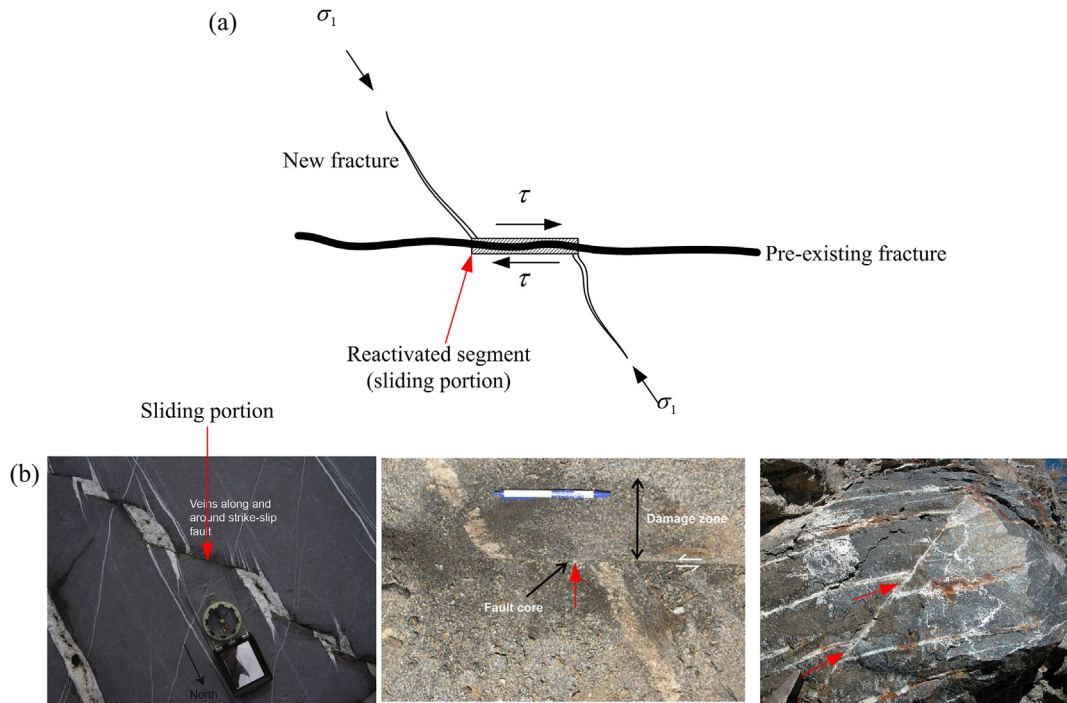
Fig. 14. The model and field observations: (a) Model for understanding the relationship between fractures and the maximum principal stress; and (b) Field observations of extension fractures formed after a slip on the pre-existing fracture surface. Photos are modified from Peacock and Sanderson (2018), Mitchell and Faulkner (2009), and Blenkinsop (2008). σ_1 is the maximum principal stress. The red arrow indicates the sliding portion of the pre-existing fracture.

conducting uniaxial compression test to match uniaxial compressive strength, Young's modulus, and Poisson's ratio; and (3) calibration on BFSs of rock with discontinuities. The BFS is correlated to cohesion and tensile strength of SJC. The BFS of specimen at $\beta = 0°$ is largely determined by the tensile strength of SJC, whereas the BFS at $\beta = 90°$ is closely related to the cohesion of SJC. The cohesion and tensile strength of SJM are adjusted until the BFSs at all values of β are approximately equal to the experimental BFSs. The microparameters of FJM are listed in Table 4. The mechanical properties of intact specimens are listed in Table 5. The relative error is less than 3.13%, which indicates that the adopted microproperties can well reproduce the mechanical behavior of rock in this study. After inserting a discontinuity at different load-discontinuity angles in the disc specimen, it is then used to

calibrate the mechanical properties of the fractured specimen. The calibrated microparameters of SJM are listed in Table 4.

Fig. 12 shows the comparisons among the numerical and experimental BFSs, and the tensile stress at the disc center. The tensile stress σ_{xx0} of the disc center at failure is often regarded as the disc tensile strength under Brazilian test conditions. In this study, σ_{xx0} is the average value of three measurement spheres located at the center in numerical tests (Li et al., 2020b). As shown in Fig. 12, BFS can reasonably represent the tensile resistance of specimens with a discontinuity. Other investigations on specimens with discontinuities have also drawn this conclusion (Tavallali and Vervoort, 2010a, b; Roy et al., 2017; Feng et al., 2020). In addition, numerical studies under Brazilian test conditions have shown that, although shear failure contributes to initial microcracking, the
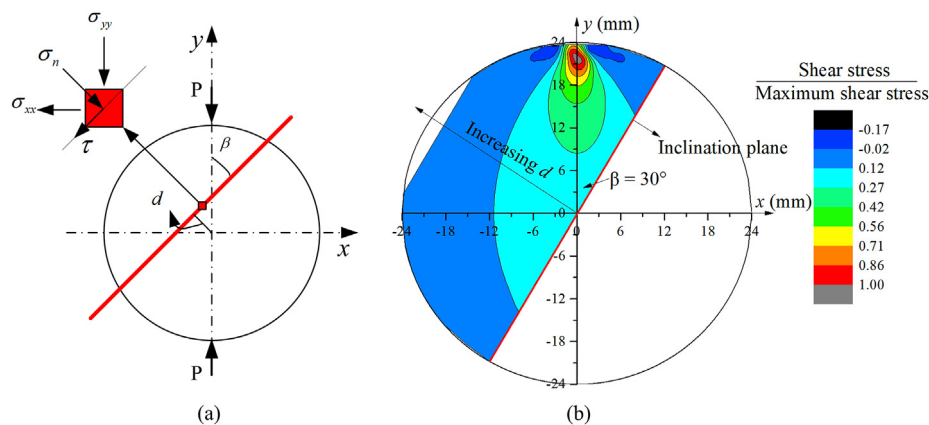
Fig. 15. Shear stress on the plane at an inclination angle β: (a) Shear stress state; and (b) Analytical solution of shear stress distribution on the inclination plane at $\beta=30°$ when d increases from 0 mm to 22 mm. The applied force $P = 10$ kN. σ_{xx} and σ_{yy} are the horizontal and vertical stresses obtained from the isotropic closed-form solution of stress distribution under Brazilian test conditions (Claesson and Bohloli, 2002; Ma et al., 2018).

failure of rock with discontinuities is mainly dominated by tension (Xu et al., 2018; Li et al., 2020b). Therefore, the BFS obtained with Eq. (4) can adequately represent the tensile resistance of intact and fractured rocks.

6. Discussion

Fig. 13 shows the fracture pattern of a fractured limestone disc subject to diametral load where $\beta \neq 0°$, in particular where $\beta = 30°$ and $60°$ (Fig. 10). The findings in this study suggested that only a specific segment of the pre-existing discontinuity, i.e. effective discontinuity segment, is reactivated when subject to diametral compressive loading. The sliding of the reactivated segment thus results in extension fractures at its tips. The induced fractures are close or parallel to the direction of the maximum principal stress, which can be attributed to stress concentrations caused by movement around the pre-existing discontinuity. It is believed that the interfacial fracture intensity factor controls the initiation of induced fractures, and the fracture toughness of host rock and/or insoluble materials controls their propagation, although this needs further research. The interfacial crack between two materials is governed by the elastic mismatch between the two materials (Akisanya and Fleck, 1992).

The findings in this study can provide a preliminary model to understand natural, complicated fracture networks. Fig. 14 shows the mechanism of this model and some field observations. In this model, extension fractures are formed after a slip on the reactivated segment of pre-existing fractures. This model is one of the five models that aim at understanding the relationship between discontinuities and the associated extension fractures (Blenkinsop, 2008). In nature, it is also common that specific segments of pre-existing discontinuities such as joints and faults are reactivated (Fletcher and Pollard, 1981; Peacock et al., 2018; Rotevatn and Peacock, 2018), resulting in a fracture network. Field observations (Blenkinsop, 2008; Mitchell and Faulkner, 2009; Peacock and Sanderson, 2018) determined that some extension fractures formed after a slip event, similar to those shown in Fig. 14b. The model also explains the formation mechanism of some complicated fracture networks such as brittle kink-band and en echelon calcite veins (e.g. Rispoli, 1981; Kim et al., 2001, 2003; Kattenhorn and Marshall, 2006; Peacock et al., 2017, 2018; Peacock and Sanderson, 2018; Rotevatn and Peacock, 2018).

The distance of the discontinuity to the disc center (d in Fig. 1), which is also related to the trace length of the discontinuity, might
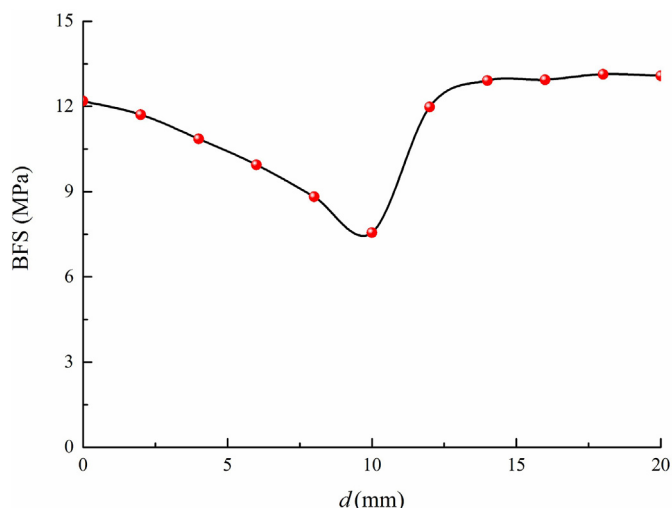

Fig. 16. Effect of d on the BFSs obtained from the numerical model test when $\beta=30°$.

be a key factor that affects the fracture process and thus the BFS of fractured limestone. Although affected by rock discontinuity, shear stress distribution in intact Brazilian disc could also provide collateral evidence. Based on the stress analysis of an infinitesimal element on the plane at an inclination angle β under Brazilian test conditions, as shown in Fig. 15a, the shear stress on this plane can be calculated as $\tau = \sigma_{xx}\sin\beta + \sigma_{yy}\cos\beta$, where σ_{xx} and σ_{yy} are the horizontal and vertical stresses, respectively, obtained from the isotropic closed-form solution of the stress distribution (Claesson and Bohloli, 2002; Ma et al., 2018). For example, under an applied force of 10 kN, Fig. 15b shows that the maximum shear stress on this plane increases when d increases from 0 to a specific value, e.g. approximately 10–12 mm at $\beta = 30°$. This indicates that the fractured specimen will be more vulnerable if shear failure is involved. Below this value, the maximum diametral load is likely to decrease with increasing d. Above this value, the maximum diametral load may increase and eventually reach a plateau. The numerical modeling results also confirm the above trend, as depicted in Fig. 16. Additionally, whether shear failure occurs depends on the weak plane shear strength, as observed by Tan et al. (2015). Therefore, the influence of d on the maximum diametral load depends on the shear strength of the discontinuity and the shear stress state on the discontinuity plane, which can be confirmed by conducting numerical model tests on specimens compromised of different discontinuity strengths. Many other factors affect the stress state, such as variations in discontinuity thickness, mechanical properties of the interface and insoluble materials, and the elastic mismatch between the host rock and insoluble materials. Further studies should be conducted by performing numerical studies to identify the influences of d on the stress distribution and fracture process. Quantified relationship between d and BFSs can also be experimentally established by conducting Brazilian disc tests on artificial rock discontinuity with known morphologies, physical and mechanical properties.

Some rock structures cannot meet the earthquake-resistance standards if accurate tensile resistance is not considered (Hashiba et al., 2017). Rock discontinuity weakens rock masses; therefore, its tensile properties play a dominant role in rock mass failure. The findings in this study provide a database for rock discontinuity tensile properties although more types of rock discontinuities should be studied. Additionally, rock discontinuity increases the plasticity of fractured rock masses, which may also play a role in reducing potential rockburst. Moreover, tensile cracks arising at the back edge of slope is part of the collapse mechanism of slope (Huang et al., 2015; Huang, 2015; Tang et al., 2017, 2019). Tensile cracks are induced by sliding due to the low tensile resistance of geomaterials. The findings in this study show that rock discontinuity can have high tensile resistance. If rock discontinuity tensile resistance was ignored, rock stability design might be inaccurate. In addition, although rock discontinuity leads to a decrease in Brazilian failure strength, it meanwhile allows an increase in tensile deformation. As slope failure often involves large deformation, rock discontinuity may reduce potential slope failure because rock discontinuity allows continuous deformation at a relatively high stress level.

7. Conclusions

The main conclusions of this study are as follows:

(1) Rock discontinuities parallel to loading direction ($\beta = 0°$) and at different load-discontinuity angles ($\beta \neq 0°$) show a more plastic deformational behavior than intact rock.
(2) The mean BFS of fractured rock increases with increasing inclination angle from $\beta = 0°$ to $\beta = 45°$. However, from

$\beta = 45°$ to $\beta = 90°$, the BFS remains almost constant, approaching that of intact rock. The SPW theory is recommended as the BFS criterion for rock with a single discontinuity.

(3) The two-parameter Weibull distribution can capture the variations in the BFS of rock discontinuity and rock specimens with a discontinuity. In addition, both the Weibull modulus and the characteristic strength are much smaller than those of intact limestone.

(4) When $\beta = 0°$, there are two types of crack paths, namely, interfacial cracks and alternative cracks. When $\beta \neq 0°$, particularly those with $\beta = 30°$ and $60°$, failure is caused by induced wing cracks at sliding discontinuity tips.

Declaration of competing interest

The authors declare that they have no known competing financial interests or personal relationships that could have appeared to influence the work reported in this paper.

Acknowledgements

References

Akisanya, A.R., Fleck, N.A., 1992. Brittle fracture of adhesive joints. Int. J. Fract. 58 (2), 93—114.

Amaral, P.M., Fernandes, J.C., Rosa, L.G., 2008. Weibull statistical analysis of granite bending strength. Rock Mech. Rock Eng. 41 (6), 917—928.

Bahaaddini, M., Sharrock, G., Hebblewhite, B.K., 2013a. Numerical investigation of the effect of joint geometrical parameters on the mechanical properties of a non-persistent jointed rock mass under uniaxial compression. Comput. Geotech. 49, 206—225.

Bahaaddini, M., Sharrock, G., Hebblewhite, B.K., 2013b. Numerical direct shear tests to model the shear behaviour of rock joints. Comput. Geotech. 51, 101—115.

Barron, K., 1971. Brittle fracture initiation in and ultimate failure of rocks: Part II — anisotropic rocks: theory. Int. J. Rock Mech. Min. Sci. Geomech. Abstr. 8 (6), 553—563.

Basu, B., Tiwari, D., Kundu, D., Prasad, R., 2009. Is Weibull distribution the most appropriate statistical strength distribution for brittle materials? Ceram. Int. 35 (1), 237—246.

Benz, W., 1994. Impact simulations with fracture I method and tests. Icarus 107 (1), 98—116.

Blenkinsop, T.G., 2008. Relationships between faults, extension fractures and veins, and stress. J. Struct. Geol. 30 (5), 622—632.

Cacciari, P.P., Futai, M.M., 2018. Assessing the tensile strength of rocks and geological discontinuities via pull-off tests. Int. J. Rock Mech. Min. Sci. 105, 44—52.

Chandler, M., Meredith, P., Brantut, N., Crawford, B., 2016. Fracture toughness anisotropy in shale. J. Geophys. Res. Solid Earth 121 (3), 1706—1729.

Chen, X., Wu, S., Zhou, J., 2014. Strength values of cementitious materials in bending and tension test methods. J. Mater. Civ. Eng. 26 (3), 484—490.

Chen, X., Wu, S., Zhou, J., 2015. Compressive strength of concrete cores under high strain rates. J. Perform. Constr. Facil. 29 (1), 1—7.

Claesson, J., Bohloli, B., 2002. Brazilian test: stress field and tensile strength of anisotropic rocks using an analytical solution. Int. J. Rock Mech. Min. Sci. 39 (8), 991—1004.

Davies, I.J., 2017a. Unbiased estimation of Weibull modulus using linear least squares analysis — a systematic approach. J. Eur. Ceram. Soc. 37 (1), 369—380.

Davies, I.J., 2017b. Unbiased estimation of the Weibull scale parameter using linear least squares analysis. J. Eur. Ceram. Soc. 37 (8), 2973—2981.

Diederichs, M.S., Kaiser, P.K., 1999. Tensile strength and abutment relaxation as failure control mechanisms in underground excavations. Int. J. Rock Mech. Min. Sci. 36 (1), 69—96.

Dirdikolu, M.H., Aktas, A., Birgören, B., 2002. Statistical analysis of fracture strength of composite materials using Weibull distribution. Turk. J. Eng. Environ. Sci. 26 (1), 45—48.

Doremus, R., 1983. Fracture statistics: a comparison of the normal, Weibull, and Type I extreme value distributions. J. Appl. Phys. 54 (1), 193—198.

Eberli, G.P., Baechle, G.T., Anselmetti, F.S., Incze, M.L., 2003. Factors controlling elastic properties in carbonate sediments and rocks. Lead. Edge 22 (7), 654—660.

Ebner, M., Piazolo, S., Renard, F., Koehn, D., 2010. Stylolite interfaces and surrounding matrix material: nature and role of heterogeneities in roughness and microstructural development. J. Struct. Geol. 32 (8), 1070—1084.

Erarslan, N., Williams, D.J., 2012. Investigating the effect of cyclic loading on the indirect tensile strength of rocks. Rock Mech. Rock Eng. 45 (3), 327—340.

Feng, G., Kang, Y., Wang, X.C., Hu, Y.Q., Li, X.H., 2020. Investigation on the failure characteristics and fracture classification of shale under Brazilian test conditions. Rock Mech. Rock Eng. 53 (7), 3325—3340.

Fletcher, R.C., Pollard, D.D., 1981. Anticrack model for pressure solution surfaces. Geology 9 (9), 419—424.

Ghazvinian, A.H., Azinfar, M.J., Geranmayeh, V.R., 2012. Importance of tensile strength on the shear behavior of discontinuities. Rock Mech. Rock Eng. 45 (3), 349—359.

Gorjan, L., Ambro, M., 2012. Bend strength of alumina ceramics : a comparison of Weibull statistics with other statistics based on very large experimental data set. J. Eur. Ceram. Soc. 32 (6), 1221—1227.

Grange, S., Forquin, P., Mencacci, S., Hild, F., 2008. On the dynamic fragmentation of two limestones using edge-on impact tests. Int. J. Impact Eng. 35, 977—991.

Griffith, A., 1921. The phenomena of rupture and flow in solids. Philos. Trans. R. Soc. A — Math. Phys. Eng. Sci. 221, 582—593.

Gurvich, M.R., Dibenedetto, A.T., Pegoretti, A., 1997. Evaluation of the statistical parameters of a Weibull distribution. J. Mater. Sci. 32 (14), 3711—3716.

Haeri, H., Shahriar, K., Marji, M.F., Moarefvand, P., 2014. Experimental and numerical study of crack propagation and coalescence in pre-cracked rock-like disks. Int. J. Rock Mech. Min. Sci. 67, 20—28.

Han, D.Y., Li, K.H., Meng, J.J., 2020a. Evolution of nonlinear elasticity and crack damage of rock joint under cyclic tension. Int. J. Rock Mech. Min. Sci. 128, 104286.

Han, D.Y., Yang, H., 2021. Effects of tensile stresses on wave propagation across stylolitic rock joints. Int. J. Rock Mech. Min. Sci. 139, 104617.

Han, D.Y., Zhu, J.B., Leung, Y.F., 2020b. Deformation of healed rock joints under tension: experimental study and empirical model. Rock Mech. Rock Eng. 53 (7), 3353—3362.

Han, D.Y., Leung, Y.F., Zhu, J.B., 2022. Tensile strength and deformational behavior of stylolites and mineral healed joints subject to dynamic direct tension. Rock Mech. Rock Eng. https://doi.org/10.1007/s00603-021-02730-6.

Hashiba, K., Okada, T., Tani, K., Shirasagi, S., Hayano, K., Nakamura, T., Oikawa, Y., Ono, M., Shimamoto, K., Yamada, S., Wakabayashi, N., Namikawa, T., Nishikane, Y., 2017. Literature survey and experimental study on the direct tension test on rocks. Geotech. Test J. 40 (2), 335—344.

Heap, M.J., Baud, P., Reuschlé, T., Meredith, P.G., 2014. Stylolites in limestones: barriers to fluid flow? Geology 42 (1), 51—54.

Hobbs, D.W., 1967. Rock tensile strength and its relationship to a number of alternative measures of rock strength. Int. J. Rock Mech. Min. Sci. Geomech. Abstr. 4 (1), 115—127.

Huang, D., Cen, D., Ma, G., Huang, R., 2015. Step-path failure of rock slopes with intermittent joints. Landslides 12 (5), 911—926.

Huang, R.Q., 2015. Understanding the mechanism of large-scale landslides. In: Lollino, G., Giordan, D., Crosta, G.B., Corominas, J., Azzam, R., Wasowski, J., Sciarra, N. (Eds.), Engineering Geology for Society and Territory — Volume 2: Landslide Processes. Springer, Cham, Switzerland, pp. 13—32.

ISRM (International Society for Rock Mechanics), 1978. Suggested methods for determining tensile strength of rock materials. Int. J. Rock Mech. Min. Sci. Geomech. Abstr. 15, 99—103.

Jayatilaka, A., Trustrum, K., 1977. Statistical approach to brittle fracture. J. Mater. Sci. 12 (7), 1426—1430.

Kattenhorn, S.A., Marshall, S.T., 2006. Fault-induced perturbed stress fields and associated tensile and compressive deformation at fault tips in the ice shell of Europa: implications for fault mechanics. J. Struct. Geol. 28 (12), 2204—2221.

Kim, Y., Andrews, J.R., Sanderson, D.J., 2001. Reactivated strike-slip faults: examples from north Cornwall, UK. Tectonophysics 340 (3—4), 173—194.

Kim, Y., Peacock, D.C.P., Sanderson, D.J., 2003. Mesoscale strike-slip faults and damage zones at Marsalforn, Gozo Island, Malta. J. Struct. Geol. 25 (5), 793—812.

Lane, M., 2003. Interface fracture. Annu. Rev. Mater. Res. 33 (1), 29—54.

Lawn, B., 1993. Fracture of Brittle Solids. Cambridge University Press, Cambridge, UK.

Lee, H.P., Olson, J.E., Holder, J., Gale, J.F.W., Myers, R.D., 2015. The interaction of propagating opening mode fractures with preexisting discontinuities in shale. J. Geophys. Res. Solid Earth 120, 169—181.

Lee, Y.K., Pietruszczak, S., 2015. Tensile failure criterion for transversely isotropic rocks. Int. J. Rock Mech. Min. Sci. 79, 205—215.

Li, K.H., Cheng, Y.M., Fan, X., 2018. Roles of model size and particle size distribution on macro-mechanical properties of Lac du Bonnet granite using flat-joint model. Comput. Geotech. 103, 43—60.

Li, K.H., Cheng, Y.M., Yin, Z.Y., Han, D.Y., Meng, J.J., 2020a. Size effects in a transversely isotropic rock under Brazilian tests: Laboratory testing. Rock Mech. Rock Eng. 53 (6), 2623—2642.

Li, K.H., Yin, Z.Y., Cheng, Y.M., Cao, P., Meng, J.J., 2020b. Three-dimensional discrete element simulation of indirect tensile behaviour of a transversely isotropic rock. Int. J. Numer. Anal. Methods GeoMech. 44 (13), 1812—1832.

Li, K.H., Yin, Z.Y., Han, D.Y., Fan, X., Cao, R.H., Lin, H., 2021. Size effect and anisotropy in a transversely isotropic rock under compressive conditions. Rock Mech. Rock Eng. 54 (9), 4639–4662.

Li, K., Han, D., Fan, X., Yang, Y., Wang, F., 2022. Shear rupture behaviors of intact and granulated Wombeyan marble with the flat-jointed model. Arch. Civ. Mech. Eng. 22 (1), 1–21.

Lu, C., Danzer, R., Fischer, F.D., 2002. Fracture statistics of brittle materials: Weibull or normal distribution. Phys. Rev. E. 65 (6), 067102.

Ma, T.S., Peng, N., Zhu, Z., Zhang, Q.B., Yang, C.H., Zhao, J., 2018. Brazilian tensile strength of anisotropic rocks: review and new insights. Energies 11 (2), 304.

Mas Ivars, D., Pierce, M.E., Darcel, C., Reyes-Montes, J., Potyondy, D.O., Paul, Y.R., Cundall, P.A., 2011. The synthetic rock mass approach for jointed rock mass modelling. Int. J. Rock Mech. Min. Sci. 48 (2), 219–244.

Mellor, M., Hawkes, I., 1971. Measurement of tensile strength by diametral compression of discs and annuli. Eng. Geol. 5 (3), 173–225.

Mitchell, T.M., Faulkner, D.R., 2009. The nature and origin of off-fault damage surrounding strike-slip fault zones with a wide range of displacements: a field study from the Atacama fault system, northern Chile. J. Struct. Geol. 31 (8), 802–816.

Nakamura, A.M., Michel, P., Setoh, M., 2007. Weibull parameters of Yakuno basalt targets used in documented high-velocity impact experiments. J. Geophys. Res. 112, 1–7.

Nelson, R.A., 1981. Significance of fracture sets associated with stylolite zones. Am. Assoc. Petrol. Geol. Bull. 65 (11), 2417–2425.

Nicolas, A., 1987. Principles of Rock Deformation. Springer, Dordrecht, Netherlands.

Nohut, S., 2014. Influence of sample size on strength distribution of advanced ceramics. Ceram. Int. 40 (3), 4285–4295.

Nohut, S., Lu, C., 2012. Fracture statistics of dental ceramics : discrimination of strength distributions. Ceram. Int. 38 (6), 4979–4990.

Nova, R., Zaninetti, A., 1990. An investigation into the tensile behaviour of a Schistose rock. Int. J. Rock Mech. Min. Sci. Geomech. Abstr. 27 (4), 231–242.

Ozaki, S., Aoki, Y., Osada, T., Takeo, K., Nakao, W., 2018. Finite element analysis of fracture statistics of ceramics: effects of grain size and pore size distributions. J. Am. Ceram. Soc. 101 (7), 3191–3204.

Paterson, M.S., Wong, T.F., 2005. Experimental Rock Deformation – the Brittle Field. Springer, Berlin-Heidelberg, Germany.

Peacock, D.C.P., Nixon, C.W., Rotevatn, A., Sanderson, D.J., Zuluaga, L.F., 2017. Interacting faults. J. Struct. Geol. 97, 1–22.

Peacock, D.C.P., Sanderson, D.J., 2018. Structural analyses and fracture network characterisation: seven pillars of wisdom. Earth Sci. Rev. 184, 13–28.

Peacock, D.C.P., Sanderson, D.J., Rotevatn, A., 2018. Relationships between fractures. J. Struct. Geol. 106, 41–53.

Rispoli, R., 1981. Stress fields about strike-slip faults inferred from stylolites and tension gashes. Tectonophysics 75, T29–T36.

Rotevatn, A., Peacock, D.C.P., 2018. Strike-slip reactivation of segmented normal faults : implications for basin structure and fluid flow. Basin Res. 30 (6), 1264–1279.

Roy, G.D., Singh, T.N., Kodikara, J., 2017. Influence of joint anisotropy on the fracturing behavior of a sedimentary rock. Eng. Geol. 228, 224–237.

Shang, J., Hencher, S.R., West, L.J., 2016. Tensile strength of geological discontinuities including incipient bedding, rock joints and mineral veins. Rock Mech. Rock Eng. 49 (11), 4213–4225.

Sharafisaf, M., Shen, L., Zheng, Y., Xiao, J., 2019. The effect of flaw filling material on the compressive behaviour of 3D printed rock-like discs. Int. J. Rock Mech. Min. Sci. 117, 105–117.

Tan, X., Konietzky, H., Frühwirt, T., Dan, D.Q., 2015. Brazilian tests on transversely isotropic rocks: Laboratory testing and numerical simulations. Rock Mech. Rock Eng. 48 (4), 1341–1351.

Tang, C., Kaiser, P.K., 1998. Numerical simulation of cumulative damage and seismic energy release during brittle rock failure – Part I : Fundamentals. Int. J. Rock Mech. Min. Sci. 35 (2), 113–121.

Tang, L., Zhao, Z., Luo, Z., Sun, Y., 2019. What is the role of tensile cracks in cohesive slopes? J. Rock Mech. Geotech. Eng. 11 (2), 314–324.

Tang, S., Huang, R., Tang, C., Liang, Z., Heap, M., 2017. The failure processes analysis of rock slope using numerical modelling techniques. Eng. Fail. Anal. 79, 999–1016.

Tavallali, A., Vervoort, A., 2010a. Failure of layered sandstone under Brazilian test conditions: effect of micro-scale parameters on macro-scale behaviour. Rock Mech. Rock Eng. 43 (5), 641–653.

Tavallali, A., Vervoort, A., 2010b. Effect of layer orientation on the failure of layered sandstone under Brazilian test conditions. Int. J. Rock Mech. Min. Sci. 47 (2), 313–322.

Toussaint, R., Aharonov, E., Koehn, D., Gratier, J.P., Ebner, M., Baud, P., Rolland, A., Renard, F., 2018. Stylolites: a review. J. Struct. Geol. 114, 163–195.

Vandeginste, V., John, C.M., 2013. Diagenetic implications of stylolitization in pelagic carbonates, Canterbury Basin, offshore New Zealand. J. Sediment. Res. 83 (3), 226–240.

Weibull, W., 1939. A statistical theory of the strength of materials. Ingvetensk. Akad. Handl. 151, 1–45.

Weibull, W., 1951. A statistical distribution function of wide applicability. J. Appl. Mech. 18 (3), 293–297.

Wong, T.F., Wong, H.C., Chau, K.T., Tang, C.A., 2006. Microcrack statistics, Weibull distribution and micromechanical modeling of compressive failure in rock. Mech. Mater. 38 (7), 664–681.

Xu, G.W., He, C., Chen, Z.Q., Wu, D., 2018. Effects of the micro-structure and micro-parameters on the mechanical behaviour of transversely isotropic rock in Brazilian tests. Acta. Geotech. 13 (4), 887–910.

Yang, X., Kulatilake, P.H.S.W., Jing, H., Yang, S., 2015. Numerical simulation of a jointed rock block mechanical behavior adjacent to an underground excavation and comparison with physical model test results. Tunn. Undergr. Space Technol. 50, 129–142.

Zhang, L., 2010. Estimating the strength of jointed rock masses. Rock Mech. Rock Eng. 43 (4), 391–402.

Zhou, T., Zhu, J.B., Ju, Y., Xie, H.P., 2019. Volumetric fracturing behavior of 3D printed artificial rocks containing single and double 3D internal flaws under static uniaxial compression. Eng. Fract. Mech. 205, 190–204.

Zhou, T., Zhu, J.B., Xie, H.P., 2020. Mechanical and volumetric fracturing behaviour of three-dimensional printing rock-like samples under dynamic loading. Rock Mech. Rock Eng. 53 (6), 2855–2864.

Zhu, J.B., Zhou, T., Liao, Z.Y., Sun, L., Li, X.B., Chen, R., 2018. Replication of internal defects and investigation of mechanical and fracture behaviour of rock using 3D printing and 3D numerical methods in combination with X-ray computerized tomography. Int. J. Rock Mech. Min. Sci. 106, 198–212.

Dr. Jianbo Zhu is a Distinguished Professor in Shenzhen University, China. He is the Deputy Director of Institute of Deep Earth Sciences & Green Energy, and Executive Director of Guangdong Provincial Key Laboratory of Deep Earth Sciences & Geothermal Energy Exploitation. He got his BSc and MSc degrees at Sichuan University, China, and PhD degree at Swiss Federal Institute of Technology Lausanne (EPFL), Switzerland. Before joining Shenzhen University, he was a postdoctoral scholar at California Institute of Technology (Caltech), Assistant Professor at Hong Kong Polytechnic University, and Professor at Tianjin University. His research interest is rock mechanics, in particular rock dynamics, dynamic behavior and response of rock mass and underground opening, wave theories in discontinuous rock mass, and induced geological disasters such as injection induced seismicity and rockburst. He is the principal investigator (PI) of research grants of about 3 million USD from Swiss National Science Foundation, Hong Kong Research Grants Council, National Natural Science Foundation of China, etc. He has authored or co-authored over 80 papers with an H-index of 27 (Web of Science Core Collections). He is the member of editorial board of *Rock Mechanics and Rock Engineering* and *Geomechanics and Geophysics for Geo-Energy and Geo-Resources*. He is a member of the Commission on Rock Dynamics, International Society for Rock Mechanics and Rock Engineering (ISRM). He was awarded the Fellowship for Prospective Researchers from Swiss National Science Foundation (2012), and Overseas High-level Talent Recruitment Programs from China government (2014).